

# Real-Time Simulation of Asymmetry Generation in Fermion-Bubble Collisions

Marcela Carena,<sup>1,2,3,4,5,\*</sup> Ying-Ying Li,<sup>6,7,†</sup> Tong Ou,<sup>3,5,‡</sup> and Hersh Singh<sup>2,§</sup>

<sup>1</sup>*Perimeter Institute for Theoretical Physics, 31 Caroline St. N., Waterloo, Ontario N2L 2Y5, Canada*

<sup>2</sup>*Fermi National Accelerator Laboratory, Batavia, Illinois, 60510, USA*

<sup>3</sup>*Enrico Fermi Institute, University of Chicago, Chicago, Illinois, 60637, USA*

<sup>4</sup>*Kavli Institute for Cosmological Physics, University of Chicago, Chicago, Illinois, 60637, USA*

<sup>5</sup>*Department of Physics, University of Chicago, Chicago, Illinois, 60637, USA*

<sup>6</sup>*Interdisciplinary Center for Theoretical Study, University of Science and Technology of China, Hefei, Anhui 230026, China*

<sup>7</sup>*Peng Huanwu Center for Fundamental Theory, Hefei, Anhui 230026, China*

(Dated: December 16, 2024)

We perform real-time simulation of fermion-bubble scattering during a first order phase transition by which the fermions become massive. This out-of-equilibrium dynamics can generate a CP asymmetry, which is a crucial ingredient for baryon asymmetry generation in the early Universe. As a prototype, we consider a 1+1-dimensional system, for which CP is replaced by charge conjugation C. We use tensor network methods to study the C asymmetry generation outside the bubble wall induced by a complex fermion mass profile. In the asymptotic region, where reflected particles are far from the scattering point, our lattice calculations are in good agreement with perturbative calculations, but are also applicable in the nonperturbative regime. Real-time evolution of the instantaneous asymmetry generation near the collision point is also accessible within our framework and can be an order of magnitude larger than the asymptotic value. This intriguing feature may have far-reaching consequences in a full model calculation of electroweak baryogenesis. Our studies provide a necessary step for guiding quantum simulations of early universe phase transitions.

## I. INTRODUCTION

The origin of baryon asymmetry remains one of the most significant questions in particle physics. Mechanisms for baryogenesis need to satisfy the Sakharov's conditions [1]: Baryon number violation, C and CP violation, and departure from thermal equilibrium. Depending on the temperature of the Universe at which baryogenesis occurs, departure from thermal equilibrium is realized by different cosmological processes. For a high-scale baryogenesis, e.g., GUT baryogenesis [2] and leptogenesis [3], baryon asymmetry is generated at a very high temperature comparable to the Planck mass where the out-of-equilibrium dynamics is due to the expansion of the Universe. For a low-scale baryogenesis, e.g., electroweak baryogenesis (EWBG) [4], the out-of-equilibrium dynamics is caused by a strong first-order phase transition.

To effectively address out-of-equilibrium dynamics, approximations are applied at multiple stages of the theoretical calculations. Take the EWBG scenario as an example: During the strong first-order electroweak phase transition, bubbles of true vacuum form, as the Higgs field acquires a vacuum expectation values (VEV), and fermions become massive. In the presence of CP violation, particles and anti-particles are redistributed among different chiral states in the collisions with the bubble wall, resulting in a non-vanishing chiral asymmetry. This asymmetry is then converted into net baryon number through the non-

perturbative sphaleron process active in the symmetric phase, outside the bubble wall. The net baryon number generated in front of the bubble wall is subsequently transported into the broken phase as the bubble expands. If the phase transition is sufficiently strong, the sphalerons become inactive, due to the Boltzmann suppression controlled by the Higgs VEV, and the baryon asymmetry is preserved. Accurate calculations of the bubble wall profile, bubble dynamics, chiral asymmetry generation by particle-bubble collisions, and sphaleron processes present multiple challenges. These calculations often rely on various approximations, introducing significant theoretical uncertainties to the predictions of the baryon asymmetry [4–9] and other observables, such as gravitational waves emitted from phase transitions [10–13].

As quantum technology advances, the possibility of achieving fault-tolerant quantum computing systems becomes increasingly attractive, and may lead to transformative tools for tackling real-time dynamics in particle physics. Studies exploring this area are consistently emerging, see review articles [14–17]. Examples include, particle scattering problems which are hard to solve by perturbation theory [18–22], parton shower studies considering quantum interference [23–25]. Real-time simulations of out-of-equilibrium dynamics on a quantum computer may well emerge as the best computational tool for a deeper understanding of the evolution of our universe. While realistic large-scale quantum simulations are still limited by resources, classical simulations with tensor network methods have enabled real-time studies of scattering phenomenon, especially in 1+1-dimensions [32–37].

In this work, driven by our interest in computing the dynamics of EWBG, we present a real-time lattice simulation of particle-bubble scattering using tensor networks. Our

\* [mcarena@perimeterinstitute.ca](mailto:mcarena@perimeterinstitute.ca)

† [yingyingli@ustc.edu.cn](mailto:yingyingli@ustc.edu.cn)

‡ [tongou@uchicago.edu](mailto:tongou@uchicago.edu)

§ [hershsh@fnal.gov](mailto:hershsh@fnal.gov)

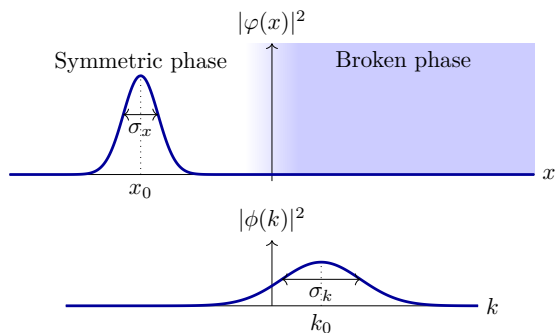


FIG. 1. Fermion (or anti-fermion) wave packet in the position space (top). The region where the color gradually changes represents the bubble wall. The wave packet in the momentum space (bottom).

efforts concentrate on a toy model in 1+1-dimensions, to explore the feasibility of realtime simulations to shed light on the realistic 3+1-dimensional scenario. In particular, we focus on the dynamics of asymmetry generation during scattering, commonly calculated with semi-classical methods [38, 39], or VEV-insertion approximation (VIA) [40–42]. Both approaches have their own limitations. Semi-classical methods only apply to walls with thickness much larger than the de Broglie wavelength of the particle, where the impact of the bubble wall can be approximated by classical force. VIA evaluates the asymmetry generation with reflection and transmission coefficients, which are only defined in the asymptotic regions away from the scattering point, and thus do not capture the instantaneous asymmetry generated near the scattering point. Moreover, the calculations of reflection and transmission coefficients are currently limited to the perturbative regime, based on expansions over the complex mass profile induced by the bubble wall within the framework of the distorted wave Born approximation (DWBA). We therefore anticipate our study to provide the first non-perturbative results on the asymmetry generation over the space throughout the scattering process. This work marks a necessary step towards simulating baryogenesis from early universe phase transitions on fault-tolerant quantum computers.

## II. CONTINUUM THEORY AND OBSERVABLES

As a prototype of chiral asymmetry generation in EWBG, we consider a Dirac fermion  $\psi$  coupled to a complex scalar field that undergoes a first-order phase transition, from the phase that preserves electroweak symmetry to the one that breaks it. Bubbles of the true vacuum of the scalar field nucleate and expand, and the massless fermions outside the bubble scatter off the wall. In the rest frame of the bubble wall, its effect on the fermions can be described by a complex mass term  $m(x) = |m(x)|e^{i\theta(x)\gamma^5}$ , where we have  $|m(x)| = 0$  in the region outside the bubble (symmetric phase  $s$ ), and a non-vanishing mass  $|m(x)| \neq 0$

inside the bubble (broken phase  $b$ ). The Hamiltonian density for the fermion is then:

$$\mathcal{H} = -i\bar{\psi}\gamma^i\partial_i\psi + |m(x)|\bar{\psi}[\cos\theta(x) + i\sin\theta(x)\gamma^5]\psi, \quad (1)$$

with the index  $i$  running over the spatial dimensions. Using the Hamiltonian in Eq. (1) we shall study the scattering of fermions with the bubble wall. While we do not consider this in our study, dynamical scalar fields can also be incorporated in our framework, such as done recently in Refs. [36, 37] to study bubble wall collisions.

The presence of a complex mass with  $\theta(x) \neq 0$  makes the scattering process qualitatively different from the case of a bubble wall profile with  $\theta(x) = 0$ . This is because a complex mass term generically breaks certain discrete symmetries relating particles and anti-particles. A non-trivial profile for  $\theta(x)$  breaks CP symmetry in 3+1-dimensions, while preserving the C symmetry. With varying  $\theta(x)$ , fermions of a certain chirality will scatter differently from their CP conjugates. One can thus measure the changes of the chiral charge density  $j_A^0 = \bar{\psi}\gamma^0\gamma^5\psi$  to quantify the effects of CP violation in scattering. Since  $j_A^0$  is CP odd, an initially CP symmetric ensemble would have a vanishing chiral charge density. However, with CP violating scattering,  $j_A^0$  would generically develop a nonzero value. This net chiral charge density subsequently creates a chemical potential that enables the electroweak sphaleron to generate more baryons than anti-baryons.

To get non-perturbative insights on this scattering process, we will analyze particle-bubble scattering within a 1+1-dimensional framework. We anticipate that the quantitative studies performed here, and the numerical extraction of asymmetry generation can be extended to CP violation in (3+1)-dimensions as quantum computational resources scale. In 1+1-dimensions, the complex-mass term breaks the charge-conjugation symmetry C but preserves CP. The transformation properties of fermion bilinears under discrete symmetries for general spacetime dimensions are discussed in Appendix A. Such symmetry breaking generates both chiral and particle number asymmetries, which in 1+1-dimensions can be measured by the C-violating chiral charge density  $j_A^0$  and particle number density  $j_V^0 = \bar{\psi}\gamma^0\psi$ , respectively. With the replacement of CP by charge-conjugation C, the discussion of measuring asymmetry generation in the previous paragraph for (3+1)-dimensions can be applied to (1+1)-dimensions.

In the scattering process relevant for generating the asymmetry near the bubble wall, a fermion particle (or its C conjugate anti-fermion particle) from the symmetric phase will move towards the bubble wall and scatter. As it becomes massive while moving from the outside to the inside of the bubble, the particle will either be reflected or transmitted. To simulate this process, we take the initial state consisting of a localized wave packet of a Weyl fermion  $|\Psi(0)\rangle_{\pm}$ , which starts in the symmetric phase and moves towards the bubble. Here  $\pm$  refers to the C conjugate pairs, such that + is for fermion, and -

for anti-fermion. The wave packet is prepared as

$$|\Psi(0)\rangle_{\pm} = \int dk \phi_{\pm}^{\text{inc}}(k) |k\rangle_{\pm}. \quad (2)$$

Here  $|k\rangle_{\pm}$  is the massless fermion (+) or anti-fermion (-) single-particle state with definite momentum  $k$  and  $\phi_{\pm}^{\text{inc}}(k)$  is the corresponding wavefunction. The wave packet in the position space is achieved via Fourier transformation. This setup for an initial Gaussian wave packet is shown in Fig. 1.  $|\Psi(0)\rangle_{\pm}$  is then evolved with the Hamiltonian in Eq. (1) to time  $t$  as  $|\Psi(t)\rangle_{\pm}$ .

The breaking of C by the bubble wall implies that particles scatter differently than the anti-particles. Therefore, we can use the total particle number in the symmetric phase as a measure of C-asymmetry generation:

$$\langle Q^s(t) \rangle_{\pm} \equiv \int_s dx \langle \Psi(t) | j_V^0(x) | \Psi(t) \rangle_{\pm}. \quad (3)$$

where the integral is performed only in the symmetric phase  $s$ , the region outside the vacuum bubble. Before scattering,  $\langle Q^s(t) \rangle_{\pm}$  is conserved at its initial value  $\langle Q^s(0) \rangle_{\pm}$ . Long after the scattering,  $\langle Q^s(t) \rangle_{\pm} |_{t \rightarrow +\infty}$  measures the total particle/anti-particle reflected by the bubble wall and should approach an asymptotic value,  $\langle Q^s(\infty) \rangle_{\pm}$ .

We obtain the analytical relation between  $\langle Q^s(\infty) \rangle_{\pm}$  and the incident wave packet by considering the reflection of a single mode  $|k\rangle_{\pm}$  incident on the wall, with its reflection coefficient  $\mathcal{R}_{\pm}(k)$ . For a real mass profile, particle and anti-particle have the same reflection coefficient at the same momentum, which we denote as  $\mathcal{R}_0(k)$ . For a localized initial wave packet in the symmetric phase,  $\langle Q^s(\infty) \rangle_{\pm}$  can be written as:

$$\langle Q^s(\infty) \rangle_{\pm} = \pm \int dk \mathcal{R}_{\pm}(k) |\phi_{\pm}^{\text{inc}}(k)|^2, \quad (4)$$

under the condition of locality of the reflected wave packet in the symmetric phase and transmitted wave packet in the broken phase at  $t \rightarrow +\infty$ . For an identical pair of fermion and anti-fermion wave packets incident on the bubble wall, i.e.,  $\phi_{+}^{\text{inc}}(k) = \phi_{-}^{\text{inc}}(k)$ , the net particle number at  $t \rightarrow +\infty$  in the symmetric phase will thus approach,

$$\begin{aligned} \langle Q^s(\infty) \rangle_{\text{net}} &= \langle Q^s(\infty) \rangle_{+} + \langle Q^s(\infty) \rangle_{-} \\ &= \int dk [\mathcal{R}_{+}(k) - \mathcal{R}_{-}(k)] |\phi_{+}^{\text{inc}}(k)|^2. \end{aligned} \quad (5)$$

For EWBG calculations, a commonly used mass profile is of the hyperbolic form [43], given by:

$$\begin{aligned} |m(x)| &= \frac{m_0}{2} \left[ 1 + \tanh \left( \frac{x - x_c}{L_w} \right) \right], \\ \theta(x) &= \frac{\theta_0}{2} \left[ 1 + \tanh \left( \frac{x - x_c}{L_w} \right) \right], \end{aligned} \quad (6)$$

where  $x_c$  is the center of the bubble wall and  $L_w$  the bubble wall width. We first consider the baseline case, where a precise analytic prediction is available. **Case I:**  $L_w \neq 0$ ,  $\theta_0 = 0$ . The reflection coefficient  $\mathcal{R}_0(k)$  for this real mass profile is given by [44],

$$\mathcal{R}_0(k) = \begin{cases} \frac{\sin[\frac{\pi}{2}(\alpha - \beta + \xi)] \sin[\frac{\pi}{2}(\alpha - \beta - \xi)]}{\sin[\frac{\pi}{2}(\alpha + \beta + \xi)] \sin[\frac{\pi}{2}(\alpha + \beta - \xi)]}, & \omega > m_0, \\ 1, & \omega \leq m_0 \end{cases}, \quad (7)$$

where  $\alpha = i\sqrt{\epsilon^2 - \xi^2}$ ,  $\beta = i\epsilon$ , with the dimensionless quantities  $\epsilon = kL_w$ ,  $\xi = m_0L_w$ .  $\langle Q^s(\infty) \rangle_{\pm}$  for a single particle or anti-particle wave packet can be obtained analytically following Eq. (4). As there is no C symmetry breaking source,  $\langle Q^s(\infty) \rangle_{\text{net}} = 0$ .

Building on the foundational setup established in the baseline case, we extend our simulations to **Case II:**  $L_w \neq 0$ ,  $\theta_0 \neq 0$ . For this case, when the complex phase  $\theta_0$  is small,  $\mathcal{R}_{\pm}(k)$  can be calculated by treating  $\theta(x)$  as a perturbation following DWBA [44], as shown in Appendix B. For large  $\theta_0$  values, DWBA breaks down and the non-perturbative real-time calculations are expected to provide different results.

### III. LATTICE SIMULATIONS

We now translate the continuum setup described in the previous section to the lattice to enable a non-perturbative study of C-asymmetry generation during fermion-bubble collisions. We then describe the results of the simulations performed using matrix product states (MPS) [45].

#### A. The lattice setup

We use staggered fermions [46] which provide a convenient doubler-free fermion formulation in 1+1-dimensions, with the following Hamiltonian defined on a  $N$ -site ( $N$  even) chain with open boundary conditions (OBC):

$$\begin{aligned} aH &= \sum_{n=1}^{N-1} i \left[ \frac{1}{2} + (-1)^n a|m_n| \sin \theta_n \right] (\chi_{n+1}^{\dagger} \chi_n - \chi_n^{\dagger} \chi_{n+1}) \\ &\quad - \sum_{n=1}^N (-1)^n a|m_n| \cos \theta_n \chi_n^{\dagger} \chi_n, \end{aligned} \quad (8)$$

where  $\chi_n$  are 1-component fermion fields,  $a$  is the lattice spacing, and  $m_n, \theta_n \equiv m(na), \theta(na)$  are discretizations of the mass profile. With the mostly-minus signature  $\eta^{\mu\nu} = \text{diag}(1, -1)$  and the choice of gamma matrices  $\gamma^0, \gamma^1, \gamma^5 = \{\sigma^3, i\sigma^2, \sigma^1\}$ , this maps to the continuum Dirac fields in Eq. (1) with  $\psi(x) = (\psi_1, \psi_2)$  as  $\chi_{2j-1} \rightarrow \sqrt{a}\psi_1(na)$  and  $\chi_{2j} \rightarrow \sqrt{a}\psi_2(na)$  for  $j = 1, 2, \dots, N/2$ . (For more details on the continuum limit, see Appendix D.) We use density matrix renormalization group (DMRG) to compute the ground state  $|\Omega\rangle$ . Usually DMRG can compute the ground state of gapped 1+1-dimensional

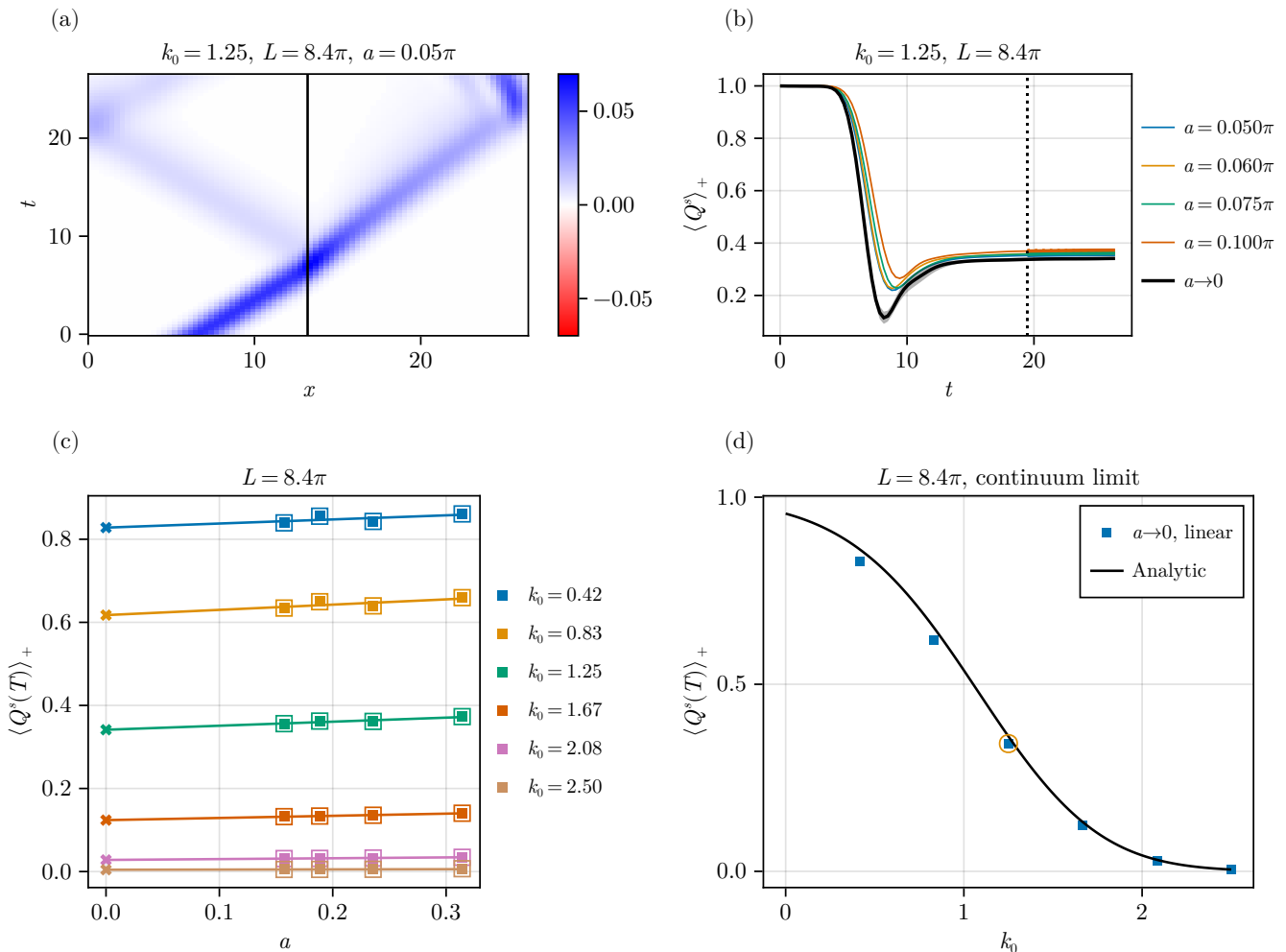


FIG. 2. Simulation results for a fermion wave packet scattering off a real mass profile. (a) Evolution of the particle number density over the lattice for  $k_0 = 1.25$  and  $a = 0.05\pi$ . (b) Particle number in the symmetric phase,  $\langle Q^s \rangle_+$ , as function of time at different lattice spacings. The vertical dotted line shows the time  $T_{3/4}$ . The solid line shows the continuum limit at time  $t$  using a linear extrapolation and the shaded band shows the  $1\sigma$  fit uncertainties. (c) Continuum limit extrapolations for  $\langle Q^s(T) \rangle_+$  using linear fit for various values  $k_0$ . The measurement errors are too small to be visible on this scale. (d) Continuum limit of  $\langle Q^s(T) \rangle_+$  as a function of  $k_0$ , compared with the analytic prediction (black line). The momentum width is fixed to  $\sigma_k = 0.52$ .

systems efficiently. Despite the vanishing mass-gap in the symmetric phase, we find that it also works very well for the system sizes considered in this work.

We prepare a Gaussian wave packet  $|\Psi(0)\rangle_{\pm} = \sum_k \phi_{\pm,k} |k\rangle_{\pm}$  with central momentum  $k_0$  and width  $\sigma_k$ , with the wave function given by:

$$\phi_{\pm,k} = \frac{1}{\mathcal{A}} e^{-ikx_0/2} e^{-(k-k_0)^2/(4\sigma_k^2)}. \quad (9)$$

The normalization factor  $\mathcal{A}$  is chosen to have  $\sum_k |\phi_{\pm,k}|^2 = 1$ . Since our calculations are performed with OBC in a fixed physical volume, the momentum modes are not well-defined. Therefore, we choose to use the periodic boundary conditions (PBC) to define the momentum modes for wave packet preparation and find

that this works well for our calculations. The exact construction of the wave packet is specified in Appendix C. Moreover, to ensure that the wave packet moves towards the bubble wall and avoids scattering with the lattice boundary in the direction opposite to the bubble, we truncate out the non-positive  $k$ -modes from the wave packet. This truncation will distort the wave packet from a perfect Gaussian shape, which will cause errors in measuring local observables. In **Case I**, we find such errors to be negligible when comparing to analytical predictions. In **Case II**, where we study the asymmetry generation, we choose  $k_0 \geq 2\sigma_k$  to ensure that the negative modes lie beyond  $2\sigma_k$  from  $k_0$ , thereby diminishing the Gaussian shape distortion.

The state  $|\Psi(0)\rangle_{\pm}$  can be time-evolved with the Hamil-

tonian in Eq. (8). The real-time evolution can be computed using a simple second-order trotter scheme as described in Appendix C using the framework of MPS, which is a good approximation as long as the entanglement does not become too large. While in general this limits the total evolution time, we find that in our simulations the errors from the MPS methods are much smaller compared to finite-volume and lattice artifacts.

On the lattice, the particle number generated in the symmetric phase indicating C-symmetry violation can be measured as,

$$\langle Q^s(t) \rangle = \sum_{n=1}^{N_c} [\langle \Psi(t) | j_{V,n}^0 | \Psi(t) \rangle - \langle \Omega | j_{V,n}^0 | \Omega \rangle], \quad (10)$$

with  $j_{V,n}^0 = \chi_n^\dagger \chi_n$  and  $N_c$  being the site index of the center of the bubble wall on the lattice. In the continuum theory, a natural scale is the mass of the fermion in the broken phase,  $m_0$ , which we use to set the scale for physical units. In the following, we report all the dimensional physical quantities in units of  $m_0$  or the correlation length  $m_0^{-1}$ . In our simulation, we will choose the bare  $m_0 = \pi/10$ .

Taking the hyperbolic mass profile in Eq. (6), we perform simulations with lattice volume  $L = 8.4\pi$ , wall width  $L_w = 0.2\pi$ , and evolution time period  $T = L$ , with the wave packet moving at the speed of light  $c = 1$  in the symmetric phase. With the center of the wall positioned at the center of the lattice,  $x_c = L_{1/2}$ , the symmetric phase can be identified as the half space with  $0 < x < L_{1/2}$ , and the broken phase as the other half with  $L_{1/2} < x < L$ . The center of the initial wave packet is positioned at  $x_0 = L_{1/4}$  to minimize the boundary effects from both the lattice boundary and the bubble wall. In this manner, the wave packet scatters with the bubble wall at  $t \sim T_{1/4}$ , after which the reflected wave packet moves towards the lattice boundary at  $x = 0$  during  $T_{1/4} < t < T_{3/4}$ , gets totally reflected by the lattice boundary at  $t = T_{3/4}$ , and moves back to its initial position at  $t = T$ , as shown in Fig. 2(a). The physical trotter step is fixed to be  $\tau = 0.01\pi$  which is much smaller than the inverse of the momentum resolution  $\Delta k = 2\pi/L$ . We will choose four different lattice spacings  $a = (0.1\pi, 0.075\pi, 0.06\pi, 0.05\pi)$  to perform the extrapolation to the continuum, for which the corresponding quantities used by the lattice simulations should be scaled appropriately by the lattice spacing, as explained in Appendix D. We take the particle number in the symmetric phase at the final time  $\langle Q^s(T) \rangle$  to be the lattice prediction for the asymptotic value  $\langle Q^s(\infty) \rangle$ .

In Appendix D, we show that the volume  $L$  is sufficiently large and the lattice spacing is sufficiently small to have well separated scales such that systematic errors in the wave packet preparation are under control. To account for errors due to finite volume effects in the measurement of  $\langle Q^s(T) \rangle$  as the asymptotic value  $\langle Q^s(\infty) \rangle$ , we take the variation of  $\langle Q^s(t) \rangle$  during  $T_{3/4} < t < T$  as the measurement error for  $\langle Q^s(\infty) \rangle$ , which is included as uncertainties in the fitting when extrapolating to the con-

tinuum. To verify the algorithm and evaluate the impact of the remaining errors, such as trotter errors, errors from momentum mode truncations, and errors from the MPS methods, we first consider the scattering with a real mass profile, and compare the lattice outcome with analytical predictions in the asymptotic region.

## B. Results for Case I: Real Mass

As particle and anti-particle propagate identically with real mass, we will only consider particle wave packets. For illustration, we show in Fig. 2(a) the evolution of a particle wave packet prepared with  $k_0 = 1.25$  and the momentum width  $\sigma_k = 0.52$  at the lattice spacing  $a = 0.05\pi$ , where the color gradient indicates the particle number density at the given spacetime point. As time evolves, we measure the particle number in the symmetric phase  $\langle Q^s(t) \rangle_+$  to track the reflection in real-time. We show  $\langle Q^s(t) \rangle_+$  at different lattice spacings in Fig. 2(b), with the vertical dashed line indicating the time  $t = T_{3/4}$ . A continuum limit of  $a \rightarrow 0$  can be reached by fitting  $\langle Q^s(t) \rangle_+$  as a function of  $a$  and extrapolating to  $a = 0$ , shown by the black line in Fig. 2(b). We observe that  $\langle Q^s(t) \rangle_+$  maintains its initial value before the wave packet hits the wall. During the scattering,  $\langle Q^s(t) \rangle_+$  drops and rises, to finally approach an asymptotic value lower than the initial one. This lower value is due to the probability of wave packet transmission into the broken phase.

To examine the momentum dependence and compare with the analytical predictions in Eq. (4), we run the simulations for a set of central momentum  $k_0$  ranging from 0.42 to 2.5. The extrapolation of  $\langle Q^s(T) \rangle_+$  to the continuum limit for different  $k_0$  is shown in Fig. 2(c) using two-parameter linear fit (solid line). The measurement errors are too small to be seen on this scale. The continuum limits of  $\langle Q^s(T) \rangle_+$  are compared with the analytic predictions in Fig. 2(d). We observe agreement between the results from our lattice extrapolations to the continuum limit and the analytic predictions obtained from Eq. (4), with a maximal relative deviation of 8% across all  $k_0$  values. Such agreement indicates the systematic uncertainties from the lattice artifacts are under control and validates the further use of our methods.

## C. Results for Case II: Complex Mass

In the following we study the scattering process in the presence of a complex mass profile. To obtain the asymmetry generated outside the bubble wall, we need to separately prepare and evolve a pair of identical particle and anti-particle wave packets. We fix the wave packet parameters  $k_0 = 2\sigma_k = 1.04$ , whereas the phase parameter  $\theta_0$  is varied in the range  $[0, 0.58\pi]$ . For two benchmarks,  $\theta_0 = 0.08\pi, 0.33\pi$ , we show the evolution of particle/antiparticle number density at lattice spacing  $a = 0.05\pi$  in Fig. 3(a). We observe temporal offsets

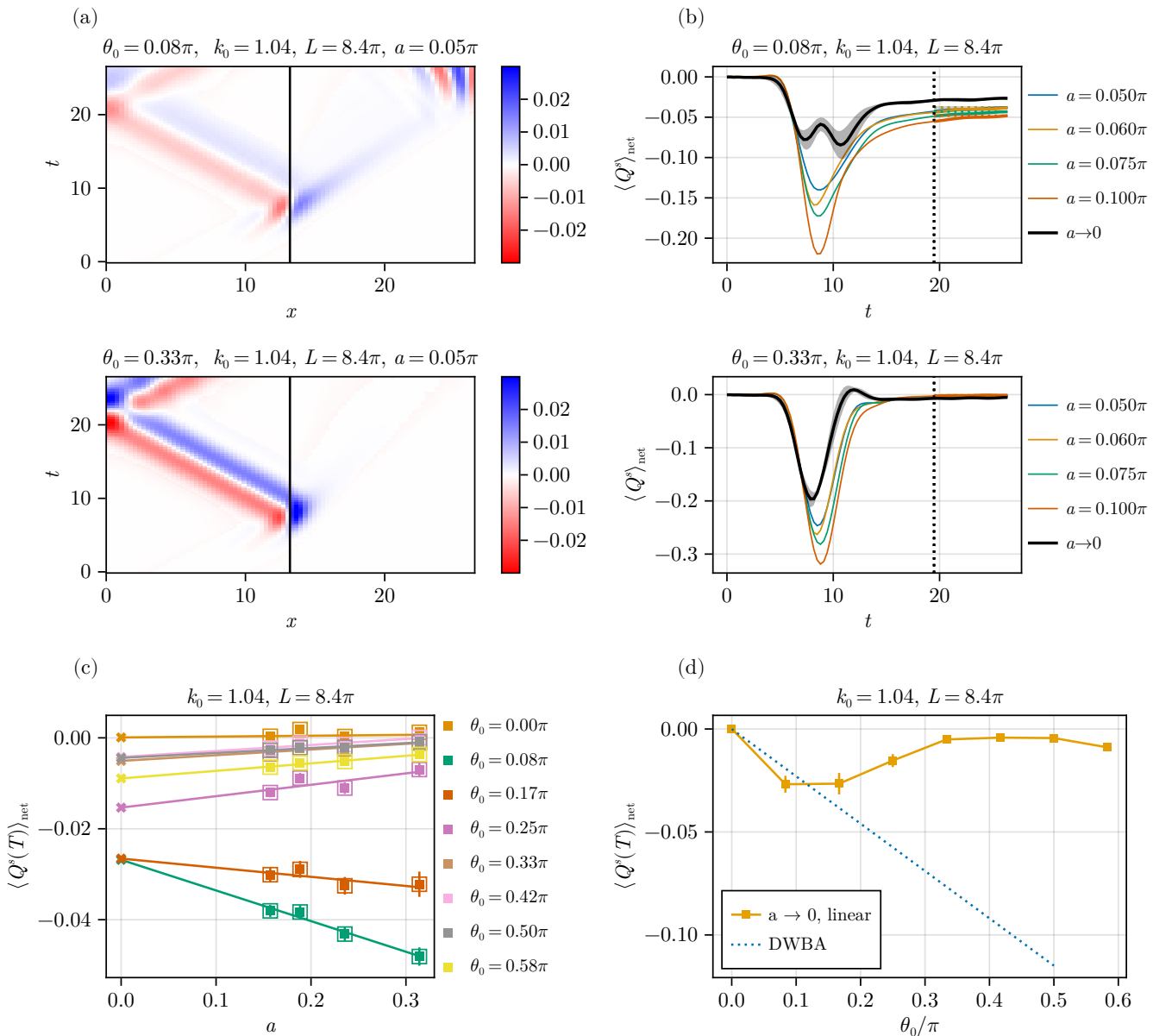


FIG. 3. Simulation results for a pair of fermion and anti-fermion scattering off a complex mass profile. For two benchmark phase parameters  $\theta_0$ , (a) shows the net particle number density in spacetime, and (b) the evolution of the net particle number in the symmetric phase  $\langle Q^s(t) \rangle_{\text{net}}$  at different lattice spacings  $a$  as well as the continuum limit extrapolation. The shaded band surrounding the continuum line represents the  $1\sigma$  uncertainty band derived from fitting uncertainty. (c) Continuum limit extrapolations for  $\langle Q^s(T) \rangle_{\text{net}}$  using linear fit for various values of  $\theta_0$ . (d) Continuum limits of  $\langle Q^s(T) \rangle_{\text{net}}$  for various  $\theta_0$ , compared with the perturbative prediction at leading order of  $\theta(x)$  (blue dashed). The error bars represent the  $1\sigma$  fitting uncertainty.

between the reflections of particle and anti-particle wave packets in the presence of a complex mass, which result in local asymmetry generation near the scattering point. For  $\theta_0 = 0.33\pi$ , both particle and anti-particle wave packets are almost completely reflected. We note that this strong reflection is correlated with large absolute values of the imaginary component of the mass term in the broken phase, for fixed  $m_0$  values. Further investigation of this

behavior is left for future work.

Summing over particle and anti-particle contributions, we show in Fig. 3(b) the net particle number  $\langle Q^s(t) \rangle_{\text{net}}$  for different lattice spacings as well as for the continuum limit from linear extrapolation. Considering the two benchmark values,  $\theta_0 = 0.08\pi, 0.33\pi$ , we observe that  $\langle Q^s(t) \rangle_{\text{net}}$  is zero at  $t = 0$ , since the initial state is symmetric under charge conjugation. As the wave packets scatter with

the bubble wall,  $\langle Q^s(t) \rangle_{\text{net}}$  first drops to a minimum, then gradually increases and approaches an asymptotic value. For the small value of  $\theta_0 = 0.08\pi$ ,  $\langle Q^s(\infty) \rangle_{\text{net}}$  approaches a non-zero asymptotic value. For  $\theta_0 = 0.33\pi$ , instead,  $\langle Q^s(\infty) \rangle_{\text{net}}$  approaches a very small value, close to zero. Such small effects of asymmetry generation in the asymptotic region may be due to the strong reflection of both particle and anti-particle wave packets in Fig. 3(a).

It is of special interest to observe in Fig. 3(b) the behavior of the instantaneous asymmetry generated in real-time near the scattering point. The results show an instantaneous asymmetry that can be an order of magnitude larger than the asymptotic value. In EWBG, the analogous CP asymmetry in 3+1 dimensions can be converted to baryon asymmetry by the  $SU(2)$  sphalerons active in the symmetric phase. The baryon asymmetry generated in the proximity of the bubble wall penetrates into the broken phase as the bubble expands and is preserved due to the inactive electroweak sphalerons if the phase transition is sufficiently strong. Thus the instantaneous CP asymmetry generated near the wall, at the collision point, may play a relevant role in predicting the observed baryon asymmetry of the universe and needs to be carefully considered in future non-perturbative studies.

For all  $\theta_0$  values in the range  $[0, 0.58\pi]$ , we show the continuum limits of  $\langle Q^s(\infty) \rangle_{\text{net}}$  obtained from linear extrapolation in Fig. 3(c), and compare with the leading-order predictions from DWBA by treating  $\theta(x)$  as perturbation (blue dashed line) in Fig. 3(d). The asymptotic values at small  $\theta_0$  match the perturbative predictions within  $3\sigma$ . The asymptotic values at larger  $\theta_0$ , instead, deviate from the perturbative predictions, as expected.

#### IV. CONCLUSION AND OUTLOOK

In this work, we perform real-time lattice simulations of fermion-bubble scattering – a process that can generate the necessary CP asymmetry to seed the observed baryon asymmetry. The simulation framework includes preparing the initial fermion wave packet, encoding the presence of the bubble wall through a fermion mass that varies across it, and computing the reflection coefficient as the fermion scatters into the wall. We perform real-time evolution via second-order trotterization, and develop observables to measure real-time scattering dynamics which leads to asymmetry generation. Using tensor network methods, we simulate charge asymmetry generation in

a 1+1-dimensional system, which is a prototype for CP asymmetry generation in a 3+1-dimensional system.

Our simulations consider both real and complex fermion mass profiles. For the former, after extrapolation to the continuum limit, our results reproduce the analytical predictions for the reflected net particle number in the symmetric phase, thereby validating our methodology. Extending the simulation for a generic complex mass profile with finite wall width, we study the fermion-bubble scattering dynamics in real-time, including the case of sizable phases for which the perturbative expansion is not valid. For different lattice spacings, we measure the net particle number densities in spacetime and compute the evolution of the total net particle number that represents the charge asymmetry in the symmetric phase. This real-time simulation shows an interesting behavior of the instantaneous asymmetry generated near the scattering point, which in its analogous 3+1-dimensional case may have important consequences for EWBG. For large values of the phase parameter, our continuum limit extrapolation of the generated charge asymmetry shows a significant disagreement with the perturbative predictions.

The results of this paper show the importance of lattice real-time simulations in evaluating the asymmetry generation in the presence of a fermion-bubble wall scattering during a first order phase transition. We expect our calculations to guide simulations of (3+1)-dimensional systems, as well as extensions to finite temperature environments, paving the way towards quantum simulations of early universe out-of-equilibrium dynamics.

#### ACKNOWLEDGMENTS

We would like to thank Henry Lamm for many useful conversations. TO is supported by the Visiting Scholars Program of URA at Fermilab and the DOE Office of Science Distinguished Scientist Fellows Award 2022. HS and MC (partially), are supported by the Department of Energy through the Fermilab QuantiSED program in the area of “Intersections of QIS and Theoretical Particle Physics.” Fermilab is operated by Fermi Research Alliance, LLC under Contract No. DE-AC02-07CH11359 with the United States Department of Energy. MC research at Perimeter Institute is supported in part by the Government of Canada through the Department of Innovation, Science and Economic Development, and by the Province of Ontario through the Ministry of Colleges and Universities.

- 
- [1] A. D. Sakharov, Violation of CP Invariance, C asymmetry, and baryon asymmetry of the universe, *Pisma Zh. Eksp. Teor. Fiz.* **5**, 32 (1967).
  - [2] D. V. Nanopoulos and S. Weinberg, Mechanisms for Cosmological Baryon Production, *Phys. Rev. D* **20**, 2484 (1979).
  - [3] M. Yoshimura, Origin of Cosmological Baryon Asymmetry, *Phys. Lett. B* **88**, 294 (1979).
  - [4] A. G. Cohen, D. B. Kaplan, and A. E. Nelson, Progress in Electroweak Baryogenesis, *Annual Review of Nuclear and Particle Science* **43**, 27 (1993), arXiv:hep-ph/9302210.

- [5] A. Linde, Infrared problem in the thermodynamics of the yang-mills gas, *Physics Letters B* **96**, 289 (1980).
- [6] D. Curtin, P. Meade, and H. Ramani, Thermal Resummation and Phase Transitions, *Eur. Phys. J. C* **78**, 787 (2018), [arXiv:1612.00466 \[hep-ph\]](#).
- [7] S. Baum, M. Carena, N. R. Shah, C. E. M. Wagner, and Y. Wang, Nucleation is more than critical: A case study of the electroweak phase transition in the nmssm, *Journal of High Energy Physics* **2021**, 55 (2021).
- [8] J. M. Cline and K. Kainulainen, Electroweak baryogenesis at high bubble wall velocities, *Phys. Rev. D* **101**, 063525 (2020), [arXiv:2001.00568 \[hep-ph\]](#).
- [9] L. Niemi, M. J. Ramsey-Musolf, and G. Xia, *Nonperturbative study of the electroweak phase transition in the real scalar singlet extended standard model* (2024), [arXiv:2405.01191 \[hep-ph\]](#).
- [10] C. Caprini et al., Science with the space-based interferometer eLISA. II: Gravitational waves from cosmological phase transitions, *JCAP* **04**, 001, [arXiv:1512.06239 \[astro-ph.CO\]](#).
- [11] C. Caprini et al., Detecting gravitational waves from cosmological phase transitions with LISA: an update, *JCAP* **03**, 024, [arXiv:1910.13125 \[astro-ph.CO\]](#).
- [12] H.-K. Guo, K. Sinha, D. Vagie, and G. White, Phase Transitions in an Expanding Universe: Stochastic Gravitational Waves in Standard and Non-Standard Histories, *JCAP* **01**, 001, [arXiv:2007.08537 \[hep-ph\]](#).
- [13] M. Carena, Y.-Y. Li, T. Ou, and Y. Wang, Anatomy of the electroweak phase transition for dark sector induced baryogenesis, *JHEP* **02**, 139, [arXiv:2210.14352 \[hep-ph\]](#).
- [14] Quantum simulation for high-energy physics, *PRX Quantum* **4**, 027001 (2023).
- [15] Quantum computing for high-energy physics: State of the art and challenges, *PRX Quantum* **5**, 037001 (2024).
- [16] C. W. Bauer, Z. Davoudi, N. Klco, and M. J. Savage, Quantum simulation of fundamental particles and forces, *Nature Rev. Phys.* **5**, 420 (2023), [arXiv:2404.06298 \[hep-ph\]](#).
- [17] Y. Fang, C. Gao, Y.-Y. Li, J. Shu, Y. Wu, H. Xing, B. Xu, L. Xu, and C. Zhou, Quantum Frontiers in High Energy Physics (2024), [arXiv:2411.11294 \[hep-ph\]](#).
- [18] S. P. Jordan, K. S. M. Lee, and J. Preskill, Quantum Computation of Scattering in Scalar Quantum Field Theories, *Quant. Inf. Comput.* **14**, 1014 (2014), [arXiv:1112.4833 \[hep-th\]](#).
- [19] Y. Chai, A. Crippa, K. Jansen, S. Kühn, V. R. Pascauzzi, F. Tacchino, and I. Tavernelli, *Fermionic wave packet scattering: A quantum computing approach* (2024), [arXiv:2312.02272 \[hep-lat, physics:quant-ph\]](#).
- [20] E. R. Bennowitz, B. Ware, A. Schuckert, A. Lerose, F. M. Surace, R. Belyansky, W. Morong, D. Luo, A. De, K. S. Collins, O. Katz, C. Monroe, Z. Davoudi, and A. V. Gorshkov, *Simulating Meson Scattering on Spin Quantum Simulators* (2024), [arXiv:2403.07061 \[cond-mat, physics:hep-ph, physics:nucl-th, physics:quant-ph\]](#).
- [21] E. R. Bennowitz et al., *Simulating Meson Scattering on Spin Quantum Simulators* (2024), [arXiv:2403.07061 \[quant-ph\]](#).
- [22] R. C. Farrell, M. Illa, A. N. Ciavarella, and M. J. Savage, Quantum Simulations of Hadron Dynamics in the Schwinger Model using 112 Qubits [10.48550/arXiv.2401.08044](#) (2024), [arXiv:2401.08044 \[quant-ph\]](#).
- [23] C. W. Bauer, W. A. de Jong, B. Nachman, and D. Provasoli, Quantum Algorithm for High Energy Physics Simulations, *Phys. Rev. Lett.* **126**, 062001 (2021), [arXiv:1904.03196 \[hep-ph\]](#).
- [24] K. Bepari, S. Malik, M. Spannowsky, and S. Williams, Quantum walk approach to simulating parton showers, *Phys. Rev. D* **106**, 056002 (2022), [arXiv:2109.13975 \[hep-ph\]](#).
- [25] C. W. Bauer, S. Chigusa, and M. Yamazaki, Quantum parton shower with kinematics, *Phys. Rev. A* **109**, 032432 (2024), [arXiv:2310.19881 \[hep-ph\]](#).
- [26] T. Bhattacharya, A. J. Buser, S. Chandrasekharan, R. Gupta, and H. Singh, Qubit regularization of asymptotic freedom, *Phys. Rev. Lett.* **126**, 172001 (2021), [arXiv:2012.02153 \[hep-lat\]](#).
- [27] M. Carena, H. Lamm, Y.-Y. Li, and W. Liu, Lattice Renormalization of Quantum Simulations (2021), [arXiv:2107.01166 \[hep-lat\]](#).
- [28] C. W. Bauer and D. M. Grabowska, Efficient Representation for Simulating U(1) Gauge Theories on Digital Quantum Computers at All Values of the Coupling (2021), [arXiv:2111.08015 \[hep-ph\]](#).
- [29] D. M. Grabowska, C. Kane, B. Nachman, and C. W. Bauer, Overcoming exponential scaling with system size in Trotter-Suzuki implementations of constrained Hamiltonians: 2+1 U(1) lattice gauge theories (2022), [arXiv:2208.03333 \[quant-ph\]](#).
- [30] C. Kane, D. M. Grabowska, B. Nachman, and C. W. Bauer, Efficient quantum implementation of 2+1 U(1) lattice gauge theories with Gauss law constraints (2022), [arXiv:2211.10497 \[quant-ph\]](#).
- [31] A. N. Ciavarella and C. W. Bauer, Quantum Simulation of SU(3) Lattice Yang Mills Theory at Leading Order in Large N (2024), [arXiv:2402.10265 \[hep-ph\]](#).
- [32] M. Van Damme, L. Vanderstraeten, J. De Nardis, J. Haegeman, and F. Verstraete, Real-time scattering of interacting quasiparticles in quantum spin chains, *Phys. Rev. Res.* **3**, 013078 (2021).
- [33] M. Rigobello, S. Notarnicola, G. Magnifico, and S. Montangero, Entanglement generation in (1+1)D QED scattering processes, *Phys. Rev. D* **104**, 114501 (2021), [arXiv:2105.03445 \[hep-lat\]](#).
- [34] I. Papaefstathiou, J. Knolle, and M. C. Bañuls, Real-time scattering in the lattice Schwinger model (2024), [arXiv:2402.18429 \[hep-lat\]](#).
- [35] R. G. Jha, A. Milsted, D. Neuenfeld, J. Preskill, and P. Vieira, *Real-time scattering in ising field theory using matrix product states* (2024), [arXiv:2411.13645 \[hep-th\]](#).
- [36] A. Milsted, J. Liu, J. Preskill, and G. Vidal, Collisions of false-vacuum bubble walls in a quantum spin chain, *PRX Quantum* **3**, 020316 (2022).
- [37] R. G. Jha, A. Milsted, D. Neuenfeld, J. Preskill, and P. Vieira, Real-Time Scattering in Ising Field Theory using Matrix Product States [10.48550/arXiv.2411.13645](#) (2024), [arXiv:2411.13645 \[hep-th\]](#).
- [38] M. Joyce, T. Prokopec, and N. Turok, Electroweak baryogenesis from a classical force, *Phys. Rev. Lett.* **75**, 1695 (1995), [Erratum: *Phys.Rev.Lett.* 75, 3375 (1995)], [arXiv:hep-ph/9408339](#).
- [39] J. M. Cline, M. Joyce, and K. Kainulainen, Supersymmetric electroweak baryogenesis, *JHEP* **07**, 018, [arXiv:hep-ph/0006119](#).
- [40] P. Huet and A. E. Nelson, CP violation and electroweak baryogenesis in extensions of the standard model, *Phys.*



Let. B **355**, 229 (1995), arXiv:hep-ph/9504427.

- [41] P. Huet and A. E. Nelson, Electroweak baryogenesis in supersymmetric models, *Phys. Rev. D* **53**, 4578 (1996), arXiv:hep-ph/9506477.
- [42] P. Huet and E. Sather, Electroweak baryogenesis and standard model CP violation, *Phys. Rev. D* **51**, 379 (1995), arXiv:hep-ph/9404302.
- [43] A. Ayala, J. Jalilian-Marian, L. D. McLerran, and A. P. Vischer, Scattering in the presence of electroweak phase transition bubble walls, *Phys. Rev. D* **49**, 5559 (1994), arXiv:hep-ph/9311296.
- [44] K. Funakubo, A. Kakuto, S. Otsuki, K. Takenaga, and F. Toyoda, Fermion scattering off CP violating electroweak bubble wall, *Phys. Rev. D* **50**, 1105 (1994), arXiv:hep-ph/9402204.
- [45] M. Fishman, S. R. White, and E. M. Stoudenmire, The ITensor Software Library for Tensor Network Calculations, *SciPost Phys. Codebases*, 4 (2022).
- [46] J. B. Kogut and L. Susskind, Hamiltonian Formulation of Wilson's Lattice Gauge Theories, *Phys. Rev. D* **11**, 395 (1975).
- [47] M. Stone, *Gamma matrices, Majorana fermions, and discrete symmetries in Minkowski and Euclidean signature* (2021), arXiv:2009.00518 [hep-th].
- [48] S. Sachdev, *Quantum Phase Transitions*, 2nd ed. (Cambridge University Press, 2011).
- [49] N. Hatano and M. Suzuki, Finding Exponential Product Formulas of Higher Orders, *Lect. Notes Phys.* **679**, 37 (2005), arXiv:math-ph/0506007.

## Appendix A: Symmetries

In this section, we discuss the symmetries of the staggered fermions formulation and their dynamics.

### 1. Continuum

Charge-conjugation. There are actually two definitions of charge conjugation since any charge conjugation symmetry can be transformed into another by a discrete chiral transformation. To define the charge-conjugation symmetry  $C$ , we first define unitary matrices  $C_\epsilon$  ( $\epsilon = \pm$ ), such that

$$C_\epsilon \gamma_\mu C_\epsilon^{-1} = \epsilon (\gamma_\mu)^T, \quad (\epsilon = \pm) \quad (\text{A1})$$

$$C_\epsilon \gamma_5 C_\epsilon^{-1} = \eta_5 (\gamma_5)^T, \quad (\text{A2})$$

for the Clifford algebra in even spacetime dimensions  $D$ . These matrices can be defined in any even dimension, and we refer the reader to Ref. [47] for a detailed pedagogical discussion.<sup>1</sup> The action of  $C_\epsilon$  on the ‘‘fifth’’ gamma matrix depends on the dimension, with  $\eta_5 = (-1)^{\frac{D}{2}}$ . With this

$\Gamma$	1	$\gamma^5$	$\gamma^\mu$	$\gamma^\mu \gamma^5$
$C_\epsilon$	$-\epsilon$	$-\epsilon \eta_5$	$-1$	$\eta_5$
$P$	1	$-1$	$(-1)^\mu$	$-(-1)^\mu$

TABLE I. Charge-conjugation  $C_\epsilon$  and parity  $P$  transformation properties of various fermion bilinears  $\bar{\psi}\Gamma\psi$ . The two definitions of charge conjugation correspond to  $\epsilon = \pm$ , as defined in Eqs. (A1) and (A3). The action of charge-conjugation on  $\gamma_5$  depends on the dimension and is given by  $\eta_5 = (-1)^{\frac{D}{2}}$  in  $D$  spacetime dimensions. We use the notation where  $(-1)^\mu = 1$  for  $\mu = 0$  and  $-1$  otherwise.

definition, a charge conjugation symmetry  $C$  acts on a spinor as

$$C_\epsilon : \begin{cases} \psi \rightarrow C_\epsilon \bar{\psi}^T \\ \bar{\psi} \rightarrow \epsilon \psi^T C_\epsilon^{-1} \end{cases} \quad (\text{A3})$$

where we used Eq. (A1) to obtain the action on  $\bar{\psi}$ . We can check that either choice of  $\epsilon = \pm$  leads to a symmetry of the fermion kinetic term, since it transforms as:

$$\bar{\psi} \gamma^\mu \partial_\mu \psi \xrightarrow{C_\epsilon} \epsilon \bar{\psi} (C_\epsilon^{-1} \gamma^\mu C_\epsilon)^T \partial_\mu \psi = \bar{\psi} \gamma^\mu \partial_\mu \psi. \quad (\text{A4})$$

On the other hand, a fermion mass term may not be invariant under this symmetry. A general fermion bilinear transforms as

$$\bar{\psi} \Gamma \psi \xrightarrow{C_\epsilon} \bar{\psi} (-\epsilon \Gamma_C)^T \psi. \quad (\text{A5})$$

The transformation of various mass bilinears  $\bar{\psi}\Gamma\psi$  for the  $C_\epsilon$  symmetry is given in Table I.

Parity. The massless Dirac fermion in even spacetime dimensions also has a parity symmetry  $P$ . We define this to be a symmetry which flips the sign of all the spatial coordinates. Under  $P$ , we have

$$P : \begin{cases} \psi(t, x) \rightarrow \kappa \gamma_0 \psi(t, -x) \\ \bar{\psi}(t, x) \rightarrow \bar{\psi}(t, -x) (\kappa \gamma_0)^\dagger \end{cases} \quad (\text{A6})$$

where  $\kappa = 1$  or  $\kappa = i$  such that  $(\kappa \gamma_0)^2 = 1$ , so that this is valid of any choice of signature, either Minkowski or Euclidean. One can check that this is always a symmetry of the fermion kinetic term, but not necessarily for a mass term. A general fermion bilinear transforms under parity as

$$\bar{\psi} \Gamma \psi \xrightarrow{P} \bar{\psi} \gamma_0^{-1} \Gamma \gamma_0 \psi. \quad (\text{A7})$$

The transformation of various bilinears is given in the second row of Table I.

### 2. Lattice

Charge conjugation. In 1+1 dimensions (mostly minus signature) with the basis choice  $\gamma_0, \gamma_1, \gamma_5 = \sigma_3, i\sigma_2, \sigma_1$ , we obtain the  $C_\pm$  matrices,

$$C_+ = \sigma_3, \quad C_- = \sigma_2, \quad (\text{A8})$$

<sup>1</sup> In Ref. [47] the  $C_+, C_-$  matrices are referred to as  $T$  and  $C$  matrices, respectively.

which lead to the following action of charge-conjugation  $C_{\pm}$  on the continuum Dirac fermion fields:

$$\begin{aligned} C_+ : \quad \psi &\rightarrow C_+ \gamma_0^T \psi^* = \psi^* \\ C_- : \quad \psi &\rightarrow C_- \gamma_0^T \psi^* = i\sigma_1 \psi^*. \end{aligned} \quad (\text{A9})$$

In the staggered fermion formulation, the action in Eq. (A9) implies that  $C_+$  is an onsite symmetry, while  $C_-$  mixes with translations:

$$C_+ : \quad \chi_n \rightarrow \chi_n^\dagger \quad (\text{A10})$$

$$C_- : \quad \chi_n \rightarrow i\chi_{n+1}^\dagger \quad (\text{A11})$$

One can check that, with the above definitions, the transformations for  $C_{\pm}$  in Table I are satisfied on the 1+1-dimensional lattice for our discretization of the complex mass term as in Eq. (8).

### Appendix B: Perturbative Calculation of Reflection Coefficient

The reflection coefficient calculation in 1+1-dimensions is analogous to that in 3+1-dimensions as shown in Ref. [44]. For a complex mass profile given by  $m(x) = |m(x)|e^{i\theta(x)}$  with  $|\theta(x)| \ll 1$ , we can expand the mass as,

$$m(x) = |m(x)| + i|m(x)|\theta(x) + \mathcal{O}(\theta^2). \quad (\text{B1})$$

For the perturbative calculation, we consider  $|m(x)|$  as the unperturbed profile, and  $|m(x)|\theta(x)$  as the perturbation at the first-order expansion of  $\theta(x)$ . With  $|m(x)|$  taking the tanh profile in Eq. (6), the unperturbed reflection coefficient  $\mathcal{R}_0(k)$  is given by Eq. (7). At the first-order of  $\theta(x)$ , the reflection coefficients for particle and anti-particle are given by,

$$\mathcal{R}_{\pm}(k) = \mathcal{R}_0(k) [1 \pm (\delta^{\text{refl}} + \delta^{\text{inc}})], \quad (\text{B2})$$

where the corrections  $\delta^{\text{refl}}$  and  $\delta^{\text{inc}}$  are,

$$\delta^{\text{inc}} = \frac{m_0}{2\sqrt{k^2 - m_0^2}} \left( \frac{\gamma_d(-\alpha, \beta)}{\gamma_u(\alpha, \beta)} I_2 + c.c. \right), \quad (\text{B3})$$

$$\delta^{\text{refl}} = \frac{m_0}{2\sqrt{k^2 - m_0^2}} \left( \frac{\gamma_d(-\alpha, -\beta)}{\gamma_u(\alpha, -\beta)} I_2 + c.c. \right). \quad (\text{B4})$$

Here  $\gamma_{u,d}(\alpha, \beta)$  are the coefficients for the upper (lower) unperturbed wave functions<sup>2</sup>, and are solved as:

$$\gamma_{u,d}(\alpha, \beta) = \frac{\Gamma(-\alpha + 1)\Gamma(-\beta)}{\Gamma\left(\frac{-\alpha - \beta \pm \xi}{2}\right)\Gamma\left(\frac{-\alpha - \beta \mp \xi}{2} + 1\right)}. \quad (\text{B5})$$

<sup>2</sup> The subscripts  $u/d$  for the  $\gamma$  functions and the wave functions in Eq. (B6) correspond to  $+/-$  in [44].  $+/-$  in [44] denote the eigenstates of  $\gamma^3$  with positive and negative eigenvalues. The results presented here are for 1+1-dimensional scattering, where  $u/d$  refer to the two eigenstates of the Dirac gamma matrix  $\gamma^1$ .

and  $I_2$  is given by the integral,

$$I_2 = \frac{1}{m_0} \int_{-\infty}^{\infty} dx [|m(x)|\theta(x)]' \Phi_d^{(+\alpha)}(x) \Phi_u^{(+\alpha)}(x), \quad (\text{B6})$$

with  $\Phi_{u,d}^{(+\alpha)}$  being the unperturbed wave functions of the hypergeometric form, see details in [44].

### Appendix C: Wave Packet Creation on a Lattice and Time Evolution

We prepare the wave packet in the symmetric phase as a superposition of plane waves for a massless fermion. Taking PBC for the symmetric phase, the Fourier transform takes the following form on the lattice for the staggered fermion:

$$\zeta_k = \begin{bmatrix} \zeta_1 \\ \zeta_2 \end{bmatrix}_k \equiv \frac{1}{\sqrt{N_c/2}} \sum_{j=1}^{N_c/2} \begin{bmatrix} \chi_{2j-1} e^{-i(2j-1)ak} \\ \chi_{2j} e^{-i2jak} \end{bmatrix}, \quad (\text{C1})$$

where  $N_c$  is the lattice site at the center of the bubble wall and is used to set the boundary of the symmetric phase. The momentum modes satisfying PBC take the discrete values  $k = -\frac{\pi}{2a} + j\frac{2\pi}{aN_c}$ ,  $j = 1, 2, \dots, N_c/2$ . This leads to the lattice Hamiltonian given by:

$$aH_{\text{PBC}} = \sum_k \zeta_k^\dagger \begin{pmatrix} 0 & \sin ka \\ \sin ka & 0 \end{pmatrix} \zeta_k. \quad (\text{C2})$$

We define  $(c_k, d_{-k}^\dagger)^T \equiv V_k \zeta_k^T$ , with  $V_k$  given by

$$V_k = \frac{1}{\sqrt{2}} \begin{pmatrix} 1 & \text{sign}(k) \\ -\text{sign}(k) & 1 \end{pmatrix}, \quad (\text{C3})$$

the Hamiltonian can be diagonalized as:

$$\begin{aligned} aH_{\text{PBC}} &= \sum_k \omega_k \left( c_k^\dagger c_k - d_{-k}^\dagger d_{-k} \right) \\ &= \sum_k \omega_k \left( c_k^\dagger c_k + d_{-k}^\dagger d_{-k} \right) + \text{const}, \end{aligned} \quad (\text{C4})$$

with  $\omega_k = |\sin ka|$ .  $c_k^\dagger$  and  $d_{-k}^\dagger$  can be expressed in terms of the position space operators as,

$$c_k^\dagger = \frac{1}{\sqrt{N_c}} \sum_{n=1}^{N_c} e^{ikna} [\Pi_{n0} + \text{sign}(k)\Pi_{n1}] \chi_n^\dagger, \quad (\text{C5})$$

$$d_{-k}^\dagger = \frac{1}{\sqrt{N_c}} \sum_{n=1}^{N_c} e^{ikna} [\Pi_{n1} + \text{sign}(k)\Pi_{n0}] \chi_n, \quad (\text{C6})$$

where

$$\Pi_{nl} \equiv \frac{1 - (-1)^{n+l}}{2}, \quad l = \{0, 1\}. \quad (\text{C7})$$

When acting on the vacuum,  $c_k^\dagger$  and  $d_{-k}^\dagger$  create particle and anti-particle excitations with  $P^\mu = (\omega_k, k)$ . We can

then construct the creation operators for the fermion ( $C^\dagger$ ) and anti-fermion ( $D^\dagger$ ) wave packets:

$$C^\dagger = \sum_k c_k^\dagger \phi_{+,k} = \sum_n \chi_n^\dagger \varphi_{+,n}, \quad (\text{C8})$$

$$D^\dagger = \sum_k d_k^\dagger \phi_{-,k} = \sum_n \chi_n \varphi_{-,n}, \quad (\text{C9})$$

with

$$\varphi_{+,n} = \frac{1}{\sqrt{N_c}} \sum_k \phi_{+,k} e^{ikna} [\Pi_{n0} + \text{sign}(k)\Pi_{n1}], \quad (\text{C10})$$

$$\varphi_{-,n} = \frac{1}{\sqrt{N_c}} \sum_k \phi_{-,k} e^{ikna} [\Pi_{n1} + \text{sign}(k)\Pi_{n0}]. \quad (\text{C11})$$

The initial wave packet  $|\Psi(0)\rangle_\pm$  is thus prepared by applying Eq. (C8) or Eq. (C9) to the ground state of the Hamiltonian with varying mass. Massive wave packets can be prepared following similar procedures, see e.g. [19, 33].

Staggered fermions in 1+1-dimensions can be mapped to a 1-dimensional spin chain by Jordan-Wigner transformation [48],

$$\chi_n = \left( \prod_{j<n} i\sigma_j^z \right) \sigma_n^+, \quad \chi_n^\dagger = \left( \prod_{j<n} -i\sigma_j^z \right) \sigma_n^-, \quad (\text{C12})$$

which ensures anti-commutation relations between different lattice sites. This leads to the following Hamiltonian:

$$aH = \sum_{n=1}^{N-1} h_{n,n+1} + h_N, \quad (\text{C13})$$

with  $h_N = (-1)^{N+1} a|m_N| \cos \theta_N \sigma_N^- \sigma_N^+$  and

$$h_{n,n+1} = \left[ \frac{1}{2} + (-1)^n a|m_n| \sin \theta_n \right] (\sigma_{n+1}^- \sigma_n^+ + \sigma_n^- \sigma_{n+1}^+) - (-1)^n a|m_n| \cos \theta_n \sigma_n^- \sigma_n^+. \quad (\text{C14})$$

The time evolution of this Hamiltonian can be efficiently implemented by Trotter decomposition. For our simulation, we employ second-order trotterization [49]:

$$e^{-iH\tau} \approx e^{-ih_{1,2}\hat{\tau}/2} e^{-ih_{2,3}\hat{\tau}/2} \dots e^{-ih_{N-1,N}\hat{\tau}/2} e^{-ih_N\hat{\tau}} e^{-ih_{N-1,N}\hat{\tau}/2} \dots e^{-ih_{2,3}\hat{\tau}/2} e^{-ih_{1,2}\hat{\tau}/2} + \mathcal{O}(\hat{\tau}^3), \quad (\text{C15})$$

where  $\hat{\tau} = \tau/a$  is the trotter step in lattice units (see discussions in Appendix D). The error for each time step is  $\mathcal{O}(N\hat{\tau}^3)$  for trotterizing  $H$  into  $N$  pairs of non-commuting terms. For total evolution time  $T$ , there are  $N_t = T/\tau$  trotter steps, thus the total error is  $\mathcal{O}(NN_t\hat{\tau}^3)$ .

#### Appendix D: Continuum Limit and Choice of Parameters

Since the continuum limit is controlled by the free fermion fixed point, we can use naive dimensional analysis to understand the scaling of the parameters on the

lattice. The continuum Hamiltonian density [Eq. (1)] with a complex mass profile  $m(x) = |m(x)|e^{i\theta(x)\gamma^5}$  is:

$$\mathcal{H} = -i\bar{\psi}\gamma^i\partial_i\psi + |m(x)|\bar{\psi} [\cos \theta(x) + i \sin \theta(x)\gamma^5] \psi. \quad (\text{D1})$$

The staggered fermion discrete Hamiltonian on a lattice of physical size  $L$  and lattice spacing  $a$  is [Eq. (8)]:

$$aH = \sum_{n=1}^{N-1} i \left[ \frac{1}{2} + (-1)^n a|m_n| \sin \theta_n \right] (\chi_{n+1}^\dagger \chi_n - \chi_n^\dagger \chi_{n+1}) - \sum_{n=1}^N (-1)^n a|m_n| \cos \theta_n \chi_n^\dagger \chi_n, \quad (\text{D2})$$

where  $N \equiv L/a$ ,  $m_n \equiv m(na)$ ,  $\theta_n \equiv \theta(na)$ . From this equation, we obtain the scaling of the bare parameters in the lattice theory as,

$$\hat{m}_n \equiv a|m_n|, \quad \hat{\theta}_n \equiv \theta_n. \quad (\text{D3})$$

Apart from the parameters in the Hamiltonian, we must also scale the wave packet carefully. The Gaussian wave packet is characterized by the central momentum  $k_0$ , the momentum width  $\sigma_k$ , the spatial center  $x_0$ , and the spatial width  $\sigma_x = 1/2\sigma_k$ . To take the continuum limit, we fix the continuum values of these parameters, and scale the bare lattice parameters as  $\hat{k}_0 = ak_0$ ,  $\hat{\sigma}_k = a\sigma_k$ , and  $\hat{x}_0 = x_0/a$ , in accordance with Eq. (D3). Other parameters relevant for the simulation are scaled as: wall width  $\hat{L}_w = L_w/a$ , trotter step  $\hat{\tau} = \tau/a$ .

**Choice of parameters.** A challenging aspect of this simulation is to balance the localities of the wave packet in the position and momentum spaces. In order to get a cleanly localized initial wave packet in the symmetric phase, we request:

$$0 \ll x_0 - \sigma_x < x_0 + \sigma_x \ll \frac{L}{2}. \quad (\text{D4})$$

On the other hand, we need the wave packet to also be sufficiently localized in momentum space to avoid lattice artifacts from large momentum modes, and to avoid leakage into negative momentum:

$$0 \ll k_0 - \sigma_k < k_0 + \sigma_k \ll \frac{\pi}{2a}. \quad (\text{D5})$$

We take  $x_0 = L/4$  so that the initial wave packet has minimal overlap with the left boundary at  $x = 0$  and the bubble wall at  $x = L/2$ . With this and  $\sigma_x\sigma_k = 1/2$ , the above inequalities can be satisfied if we choose the wave packet momentum-space parameters  $\sigma_k, k_0$  such that

$$\frac{\pi}{2a} \gg k_0 \gg \sigma_k \gg \frac{2}{L} = \frac{\Delta k}{\pi}. \quad (\text{D6})$$

where we set  $\Delta k = 2\pi/L$  as the resolution in momentum space. Getting a clean separation of all these scales is a numerical challenge. In particular, for a fixed  $\sigma_k$  (in physical units), we expect there would increased systematic

errors as we make  $k_0$  too small ( $k_0 \lesssim \sigma_k$ ), as well as when  $k_0$  becomes large ( $k_0 \gtrsim \pi/2a$ ).

The largest physical box for which we perform simulations is  $L = 8.4\pi \approx 26$  which gives  $\Delta k \approx 0.12$ . The largest spacing we have is  $a = \pi/10$ . Therefore, we need

$$5 \gg k_0 \gg \sigma_k \gg \Delta k/\pi \approx 0.08. \quad (\text{D7})$$

We see that a parametric separation of the scales  $k, \sigma_k$  can be satisfied with this volume, which implies that the finite volume effects from wavepacket might be small for our studies. We will fix  $\sigma_k \approx 0.52$  at all lattice spacings to perform continuum limit extrapolations.